CERN-LHCC-2003-060
LHCC-RD-003
RD Status Report/RD39
12 November 2003

RD39 STATUS REPORT

RD39 Collaboration

K. Borer, S. Janos and K. Pretzl
Laboratorium für Hochenergiephysik der Universität Bern, Sidlerstarsse 5, CH-3012 Bern, Switzerland
Ilia Britvitch, Andrei Kouznetsov, Yuri Musienko, Stephen Reucroft and John Swain,
Northeastern University, Boston, USA
Wei Chen and Zheng Li (co-spokesman)
Brookhaven National Laboratory, Upton, NY 11973-5000, USA
C. da Viá
Brunel University, Uxbridge, Middlesex UB8 3PH, UK
L. Casagrande[1], S. Grohmann[2], E. Heijne, C. Lourenço, T.O. Niinikoski (co-spokesman), G. Nuessle, V.G. Palmieri[3] and B. Perea Solano
CERN, CH-1211 Geneva, Switzerland
O. Hempel, R. Herzog and E. Wobst
ILK Dresden, Bertolt-Brecht-Allee 20, 01309 Dresden, Germany
E. Borchi, M. Bruzzi, D. Menichelli and S. Pirollo
Dipartimento di Energetica, Universitá di Firenze, I-50139 Firenze, Italy
Y. Popowski
Department de Radiologie, Universite de Geneve, CH-1211 Geneva, Switzerland
V. O'Shea, M. Rahman and G. Ruggiero[4]
Department of Physics and Astronomy, University of Glasgow, Glasgow G12 8QQ, UK
J. Härkönen, P. Luukka, E. Tuominen and E. Tuovinen
Helsinki Institute of Physics, P.O.Box 64, 00014 University of Helsinki, Finland
W. de Boer, H. Bol, A. Dierlamm, A. Furgeri, E. Grigoriev[5], F. Hauler and L. Jungermann
IEKP University of Karlsruhe, D-76128 Karlsruhe, Germany
M. Abreu, P. Rato Mendes, P. Sonderegger and P. Sousa
LIP, Av. E. Garcia, P-1000 Lisbon, Portugal
V. Cindro, I. Mandic, M. Mikuz and M. Zavrtanik
Jozef Stefan Institute, Exp. Particle Physics Dep., PO Box 3000, 1001 Ljubljana, Slovenia
O. Militaru, K. Piotrzkowski and X. Rouby
Université Catholique de Louvain, B-1348 Louvain-la-Neuve, Belgium
Rita De Masi and S. Paul
Physik Department E18, Technische Universität München, D-85748 Garching, Germany
S. Buontempo, N. D'Ambrosio and S. Pagano
Dipartimento di Fisica, Universitá "Federico II" and INFN, I-80125 Napoli, Italy
V. Eremin, I. Ilyashenko and E. Verbitskaya
Ioffe Physico-Technical Institute, Russian Academy of Sciences, St. Petersburg 194021, Russia
R. Laiho, L. Vlasenko[6] and M. Vlasenko[6]
University of Turku, Wihuri Physical Laboratory, FI-20014 Turku, Finland
P. Anbinderis, T. Anbinderis, E. Gaubas, V. Gorbatenko, V. Kalesinskas, J. Kapturauskas and J. Vaitkus
University of Vilnius, Institute of Materials Science and Applied Research, 2040 Vilnius, Lithuania

[1] Now at INFN, Section of Rome II, Italy
[2] Now at SINTEF, Trondheim, Norway.
[3] Now at HIP, Helsinki, Finland
[4] Now at CERN, Geneva, Switzerland
[5] Also at Department de Radiologie, Geneva Switzerland
[6] Also at Ioffe PTI, St. Petersburg, Russia

Summary

Significant progress has been made by the CERN RD39 Collaboration in the past year in the development of super radiation-hard cryogenic Si detectors for applications in experiments at LHC, in particular after its future luminosity upgrade. The detailed modeling of the Lazarus effect has shown that the electric field in irradiated Si detectors can be easily manipulated by the filling state of two deep defect levels at cryogenic temperatures. Advanced radiation hard detectors using charge or current injection, the current injected diodes (CID), have been developed by RD39. In a CID, the electric field is controlled by injected current, which is limited by the space charge, yielding a nearly uniform electric field in the detector, independent of the radiation fluence. Different modes of current or charge injection was studied: 1) Charge injection mode using a LED or laser as light source; 2) Ohmic current injection mode using the symmetric p/n/p structure (after radiation beyond space charge sign inversion it becomes p/"p"/p); and 3) Forward current injection mode using the p/n/n junction diode structure operated at forward bias potential. It was found that CID detectors can be operated in the temperature range of 100 K to 200 K with much improved CCE as compared to RT operation. Beam tests of the edgeless Si detectors at cryogenic temperatures have shown very good results with sensitivity up to the physical edge of the detector. New techniques to study radiation induced defects and carrier lifetime degradation, such as the defect spectroscopy using the Lazarus effect and the contactless microwave lifetime setup, have been developed. Future studies are now under way for developing ultra hard cryogenic Si detectors for the LHC upgrade, where the radiation hardness is required up to 10^{16} n_{eq}/cm^2, at which trapping will limit the charge collection depth to the range of 20 μm to 50 μm regardless of the depletion depth. The key of our approach is to use freeze-out of the trapping that affects CCE. Temperatures lower than the 80 K may be needed here. New measurement equipment with LHe cryostat, including fast TCT (with ps laser), CCE with β source, an in-situ microwave lifetime setup, will be designed and constructed in the next few months in time for the measurements of Si pad and segmented detectors at temperatures lower than 80 K.

1 INTRODUCTION

The extension of the RD39 programme was approved by LHCC in their meeting of 15-16 May 2002, with the following wording:

"The LHCC considers that the documentation fulfills the Committee's request for additional information and encourages the Collaboration to continue work on

a) understanding the phenomena of radiation damage in semiconductor devices,
b) investigating parameters influencing the charge collection efficiency, and
c) investigating larger size sensors together with the associated read-out.

The LHCC considers that the technology developed by RD39 may be potentially a very interesting option for tracking detectors in high radiation environments and recommends that the Collaboration carry out their further programme of work and submit a status report to the LHCC in one year."

The Device Physics and Basic Research projects were thus clearly recommended and approved, as well as the Cryogenic silicon detector modules project. The latter was understood to mean large pixel and strip detector modules with specifications satisfying the needs of LHC and, in particular, of future LHC upgrades in luminosity.

The Research Board concurred with the decision of LHCC in their meeting of 30 May 2002. The Common projects were suggested by RB to be dealt within the relevant committees. After a careful revision, the three Common projects have now the following status:

- RD39/NA60 terminated, remaining studies of irradiated sensors within Device Physics;
- RD39/COMPASS ongoing;
- RD39/TOTEM terminated, edgeless detector development continues under the Cryogenic Modules project.

In Section 2 of this paper we shall report the status of the Device Physics and Basic Research Projects. Although these are two separate projects with different compositions of the project teams, samples and information are intensely exchanged between them. This is reflected in their combined report. In Section 3 we shall review progress in the Cryogenic Modules project, which now also includes the Edgeless sensors. The RD39/COMPASS Common project is briefly discussed in Section 4. The plans for the projects are described in Section 5, together with estimates of resources and schedule.

2 DEVICE PHYSICS AND BASIC RESEARCH

2.1 Device Physics

The traditional approaches for improvement of silicon radiation detectors are based on the modification of the properties of silicon by doping with different impurities or lattice defects. The best results were achieved for silicon doped with oxygen (Czochralsky silicon, or silicon doped by the long term oxidation). The maximum improvement of the radiation hardness is by a factor of 2-3 for protons, but no improvement is revealed for neutron-irradiated detectors.

In the RD39 Device Physics project, new methods were developed and verified. They are based on the physical properties of the deep levels in reverse biased p/n junction (Lazarus effect) and on the basic laws of the current flow in a heavily compensated semiconductor or semi-insulator (current injected detectors, CID).

The results presented in this Subsection are divided into parts describing our main approaches for the improvement of radiation hardness. A common factor in all these cases is that the detector devices are optimised for operation at low temperatures.

a. Charge collection in strip detectors

An investigation of charge collection in non-irradiated and proton irradiated strip detectors has been carried out at the experimental setup for transient current pulse response measurements at CERN.

- A delayed component of the transient current pulse response of strip detectors has been observed and analysed. The induction delay was quantitatively explained in the framework of a simplified, one-dimensional "virtual grid" model [2.1]. A program, based on professional "IGOR" software, was developed for the calculation of the weighting potential.
- The "returned charge" effect [2.2] for the charge on the strip side was observed. For its investigation, a new design of strip detectors was developed. A field plate was implemented on the passivation layer in the inter-strip gap, and a new set of detectors with different values of strip pitch and width was processed and irradiated by 24 GeV protons at CERN. It was deduced that the "returned charge" is due to the accumulated layer of free electrons in the inter-strip gap.

The dependence of the charge cluster width on the irradiation fluence and on the operational mode was investigated experimentally. It was shown that the trapping of free carriers and the partial depletion of the detector broaden the cluster. The model developed for the cluster computation, taking into account carrier trapping and weighting potential distribution, shows a good agreement with the experimental data on the cluster.

b. The Lazarus effect study

The Lazarus effect, initially observed as a significant improvement of the charge collection efficiency for irradiated detectors in the temperature range below 150 K, was further studied in the DP project experimentally, and an analytical model of the effect was developed.

- Using the model it was demonstrated [2.3] that the CCE recovery is due to the reduction of the charged fractions of radiation induced deep donors and acceptors, which results in an increase the space charge region (SCR) depth and therefore the CCE.
- The calculation of the charged fractions for mid-gap deep donor (E_v + 0.48 eV) and deep acceptor (E_c – 0.53 eV) was performed taking into account the density of free electrons and holes, which are thermally generated in the SCR. The calculation showed that at temperatures below 140 K the space charge concentration decreases, which leads to full depletion even at low bias.

- The CCE recovery at low temperatures was directly observed using TCT in detectors irradiated by neutrons, by protons of high and medium energy, and by gamma-rays [2.3].
- A simulation program was developed for the Lazarus effect, based on this model. This was successfully applied for the treatment of numerous experimental results for detectors irradiated by different types of radiation [2.3]. The results of simulation considering specific assembly of deep levels induced by each type of radiation showed good agreement with the developed model of the Lazarus effect (see Fig. 2.1). It is shown that the deep levels responsible for the CCE recovery are identical for detectors irradiated by neutrons and protons.
- The new "zigzag" temperature dependence of the CCE with two maxima (see Fig. 2.2) was observed in detectors at lower bias potential. This particular shape has been explained by the double-peak electric field distribution in heavily irradiated detectors, and by the redistribution of the SCR depth between the depleted regions adjacent to the p^+ and n^+ contacts.
- The Lazarus effect model is important in studying the properties of the mid-gap deep level in heavily irradiated silicon. These levels are hard to detect by conventional methods. The high sensitivity of the Lazarus effect and the adequate theory allow one to use the model as a tool for the deep level study (see Section 2.2).
-

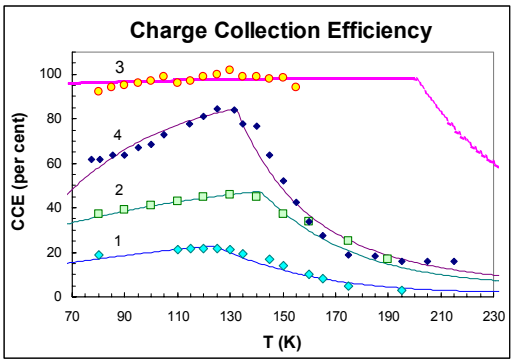

Fig. 2.1. Experimental CCE vs. *T* for MIPs for detectors irradiated by neutrons. Points – experimental data, solid lines – simulated curves. Neutron fluences (cm^{-2}): 1 – 10^{15}; 2 – $5 \cdot 10^{14}$; 3, 4 – 10^{14}. Reverse bias potential: 1, 2, 3 250 V; 4 – 100 V.

.

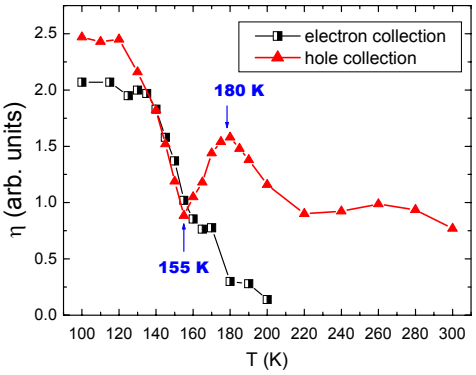

Fig. 2.2 "Zigzag"-shaped Lazarus effect for electron collection in a detector from standard Si irradiated by neutron fluence of $5.15 \cdot 10^{15}$ cm^{-2}

c. Current injected detectors

The second approach considered for the advanced radiation hard detectors is the electric field manipulation in the detector bulk using carrier injection. The physics of the injected current, named "space charge limited current" (SCLC), was investigated in insulators earlier. In this mode the current density in the bulk and the applied potential control the electric field profile, which has the following specific features:

- In the SCLC mode the electric field, at any bias and for any concentration of deep traps, is distributed in the entire volume between the contacts, and therefore the detector may stay fully depleted irrespective to its irradiation history.
- The temperature and the concentration of radiation-induced defects with deep levels are the parameters, which affect the current flow through the sample bulk. However, their influence on the electric field distribution is negligible.

In contrast to this, in junction detectors operated at reverse bias a high density of dominating acceptor type deep levels leads to the shift of the electric field maximum to the n^+ contact. This increases the full depletion potential up to 1000 V that is beyond the practical range.

The development of CIDs within the DP project work was performed in three steps:

- The design, fabrication and irradiation of the test samples;
- Investigation of I-V characteristics, of the CCE vs. *T*, and of the electric field distribution using TCT;
- Development of an analytical model of CID operation for the detector engineering.

The test samples were processed with pad, strip and pixel segmentation on n-type and p-type silicon with different resistivities, as listed in Table 1.

Structure	Type of silicon	Resistivity, kΩcm
P^+_{segm} - N – N^+	N	7
P^+_{segm} - N – N^+	N	5
P^+ - N – N^+_{segm}	N	7
P^+ - N – N^+_{segm}	N	1.2 – 2.5
N^+_{segm} – P – P^+	P	10
P^+_{segm} - N - P^+	N	10

Table 2.1: List of samples used for CID studies. The subscript "segm" indicates the side on which strip or pixel structures were processed.

The samples were irradiated by 24 GeV protons with six fluences: $6.8\cdot10^{10}$ cm^{-2}, $1.08\cdot10^{14}$ cm^{-2}, $3.2\cdot10^{14}$ cm^{-2}, $5.6\cdot10^{14}$ cm^{-2}, $8.6\cdot10^{14}$ cm^{-2}, and $3.75\cdot10^{15}$ cm^{-2}.

The full depletion potential measured on pad detectors made of 7 kΩcm n-type and 10 kΩcm p-type silicon are presented in Fig 2.3 as a function of fluence. The slopes for n- and p-type Si indicate different radiation tolerance of the material. The maximum operational fluence for p-Si (about $3\times10^{14}cm^{-2}$) is significantly lower than that for the n-Si.

The CID investigation was made using three ways of carrier injection:

- *Carrier Injection by highly absorbed light in reverse biased p/n junction*
- *Current Injection via ohmic (p/p) contact*
- *Current Injection via p-n junction*

Injection by light in $P^+ – N – N^+$ structures

It has been shown that:

- The light injection is useful for the optimisation of the electric field distribution in the active volume. Under certain conditions it allows to maintain a highly uniform electric field in the entire bulk of the detector;

- The electric field distribution is well predicted and the corresponding analytical equation was derived;
- This unique possibility, however, is technically complicated for its routine application in a large tracker.

Injection via ohmic contact in P^+ - N – P^+ structures

This approach is realized in the symmetric initial P^+-N-P^+ structures, which are converted into P^+-P-P^+ structures after irradiation beyond space charge sign inversion (SCSI). One of the P^+-P contacts injects holes under the applied potential, which then drift in the detector volume. Two modes are identified:

- At low bias potential the current flow between the contacts is controlled by the resistivity of the bulk (Ohm's law) and by the uniformly distributed electric field.
- At higher bias potential the injected current and the concentration of free holes are high enough, and the electric field is strongly disturbed by the concentration of the holes trapped by the deep levels of radiation induced defects. The electric field is equal to zero at the contact injecting the carriers and rises with depth as $x^{1/2}$ towards the opposite contact.

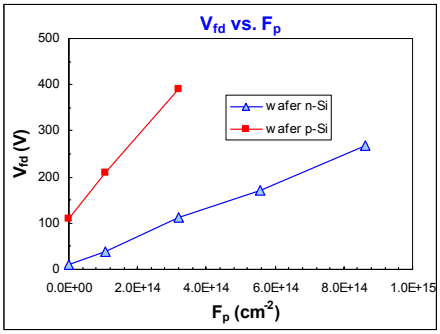

Fig. 2.3 Dependence of the full depletion potential on proton fluence for detectors processed from high resistivity n and p-type Si.

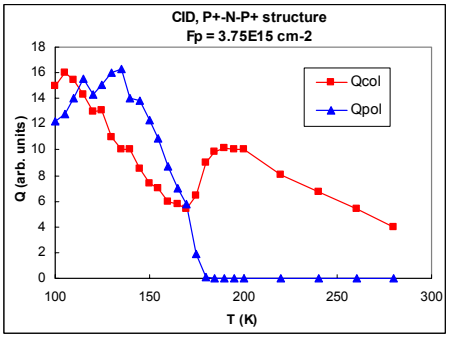

Fig. 2.4 Temperature dependence of the collected charge for proton irradiated detector based on a symmetric P^+-N–P^+ structure under applied bias of 300 V (Q_{col}) and of the charge collected in a polarization induced field at zero bias (Q_{pol}).

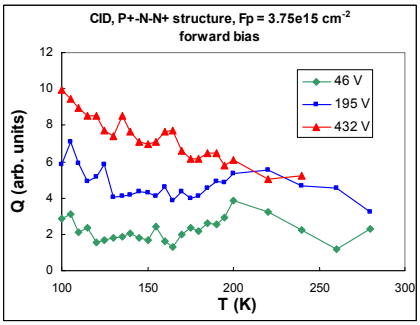

Fig. 2.5. Dependence of the collected charge on temperature illustrating monotonic increase of the charge with cooling in a junction CID at different operational bias

The temperature dependence of the collected charge for proton irradiated detectors based on a symmetric P^+-N-P^+ structure under applied bias of 300 V (Q_{col}) and of the charge collected in a polarization induced field at V = 0 (Q_{pol}) are shown in Fig. 2.4. At $T > 180$ K the structure features stable operation even at high counting rate.

It was shown that the advantage of such detector is that the range of operational bias starts at 100 V, which is significantly lower than that for the regular junction detector irradiated up to $3.7 \cdot 10^{15}$ p/cm^2. As follows from Fig 2.3, the expected full depletion potential in a junction detector irradiated to the same fluence would be higher than 1000 V.

Injection via p/n junction

This mode was realized on the $P^+ – N – N^+$ structures biased in the forward direction. The major features of the mode are:

- Elimination of the polarization is achieved since both types of free carriers are injected inside the bulk of the detector operated at a forward bias, and injected carriers recombine effectively with the carriers captured to the deep levels, which was the cause of polarization.
- The collected charge increases monotonically with cooling (Fig. 2.5) that does not create any limit for the operational temperature.

Theoretical study

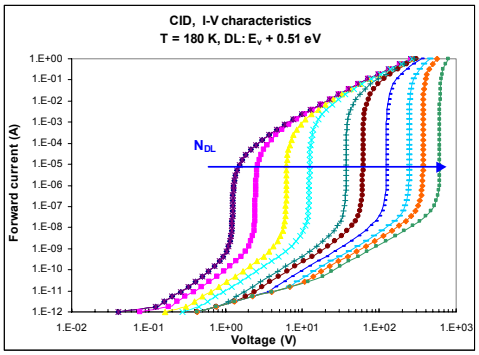

Fig. 2.6 Calculated I-V characteristics of CID at various deep level concentration. Deep level: hole trap at $E_v + 0.51$ eV. The concentration changes in the range 10^{10} to $5 \cdot 10^{12}$ cm^{-3}, its increase is shown by the arrow.

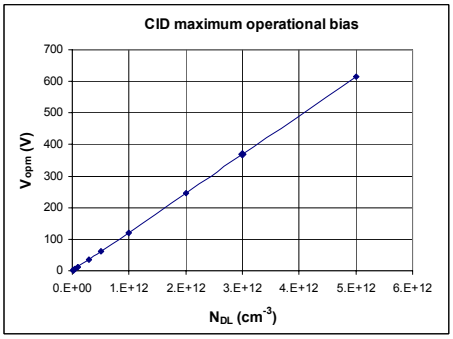

Fig. 2.7 Dependence of the maximum bias of current injected detector on proton fluence (hole injection) defined as a potential corresponding to the sharp increase of the current.

The analytical model of CID is based on the SCLC theory in solids. The model yields predictions for the main CID characteristics at a given irradiation fluence and with given parameters of deep levels. These predictions are for the current at the given temperature and the potential range that is limited by a steep current increase (Fig 2.6). The model shows that:

- The electric field is nearly uniform between the detector contacts at any fluence, temperature and bias;
- The gradient of the electric field near the injecting contact increases with accumulating fluence;

- The dependence of a maximal operational bias V_{opm} on fluence is linear (Fig 2.7), which confirms the stability of the detector with the increasing fluence.

2.2 Basic Research

a. Charge collection efficiency of highly irradiated silicon sensors at low temperatures

The model of the Lazarus effect allows the investigation of deep defects in detectors irradiated by very high fluences. The use of standard methods for such samples is often problematic. As an example, the temperature dependences of N_{eff} is presented in Fig. 2.8 for two detectors, made of standard Si and oxygenated Si and irradiated by extremely high doses ~1.7 Grad of γ-rays. For standard Si, $N_{\text{eff}}(T)$ shows non-monotonic behavior with SCSI, which is quite unique for irradiated detectors, and is related with the temperature dependence of the deep level filling. The slight increase in N_{eff} from its initial value of $-6\cdot10^{12}$ cm^{-3}, which occurs from RT to 220 K, is followed by a sharp increase up to about zero and SCSI at $T = 200$ K. The maximum positive N_{eff} of $2\cdot10^{12}$ cm^{-3} is achieved at $T \approx 190$ K after which N_{eff} goes down monotonically to a saturated value of $\sim3\cdot10^{11}$ cm^{-3}. For oxygenated Si, N_{eff} is positive at any T and at $T < 190$ K N_{eff} has the same positive value in both types of silicon detector, which indicates that the same deep levels contribute to N_{eff}.

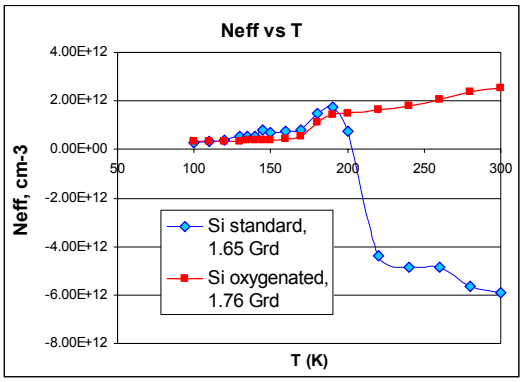

Fig. 2.8. $N_{eff}(T)$ for detectors made of standard and oxygenated Si and irradiated by an ultra-high dose of γ-rays.

The time and temperature dependences of the charge collection efficiency (CCE) of heavily irradiated standard FZ and oxygenated (93 hours in O_2 at 1200º C) FZ silicon samples have been evaluated at 100 V and 200 V reverse and forward bias from 220 K down to 95 K using the equipment at LIP Faro. Samples were irradiated at CERN with 24 GeV protons (standard) and at PSI Zürich with 192 MeV pions (oxygenated) 1.8×10^{14} cm^{-2} to 5.0×10^{14} cm^{-2} 1 MeV neutron equivalent fluences. The results obtained have been analyzed in the framework of the polarization and Lazarus effect models [2.4, 2.5].

The time dependence of the CCE in standard silicon samples showed a good agreement with the model of detector polarization by minimum ionizing particles, yielding polarization time constants larger than 50 minutes. In the case of oxygenated samples, a stabilization of the CCE was observed after the first 10 minutes after bias switch-on. This is an indication of a different polarization behavior from the one observed on standard silicon. As a consequence, after polarization the oxygenated samples present values of CCE up to a factor 2 higher than standard ones, when both types of detectors were irradiated to fluences close to

5×10^{14} n·cm^{-2} and operated under 200 V of reverse bias. No significant decrease of the CCE was observed under forward bias operation.

The temperature dependence of the CCE of standard silicon samples showed a good agreement with the Lazarus effect model, with maximum at temperatures close to 130 K and a decrease of the CCE at lower temperatures due to trapping, although not a monotonic one (always descending) after detector polarization, as would be expected from the model. In the case of oxygenated samples a more complex structure was observed, with two local maxima at temperatures close to 130 K and 175 K, and one minimum at 160 K before polarization. This structure becomes less evident after polarization, with the maximum widening and the variations becoming less intense and smoother (see [2.6] for details).

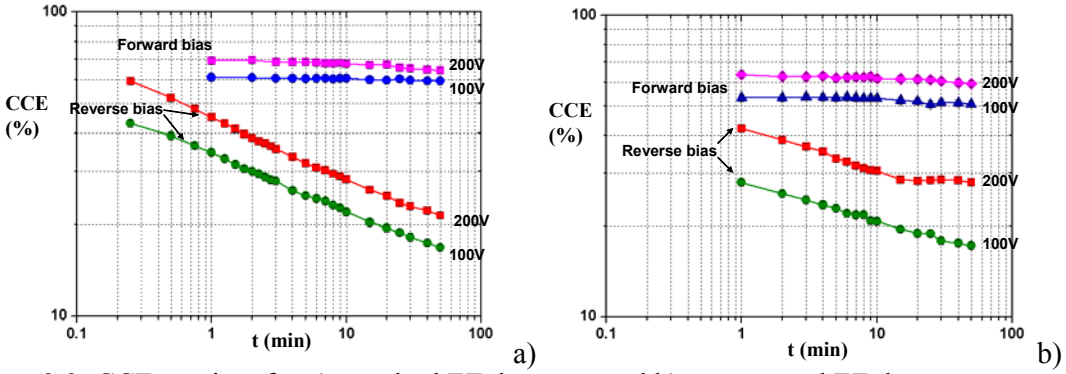

Figure 2.9: CCE vs. time for a) standard FZ detector; and b) oxygenated FZ detector

Although a good agreement between experimental data and theoretical models was observed for standard silicon samples, a deeper understanding of oxygenated material data is needed in order to have a comprehensive picture of the physics of heavily irradiated silicon at low temperatures. For standard silicon, however, consistent results on the concentrations of deep levels are given by the Lazarus effect model, accounting for the time and temperature behavior of the CCE at low temperatures [2.6]. The fitting of experimental CCE vs. *T* curves to the Lazarus effect model can be used as a new technique to obtain information on mid-band-gap deep levels in heavily irradiated Si detectors [2.6]. We intend to continue this work analyzing more data and improving the theoretical models in order to have a complete understanding of the operation of both standard and oxygenated heavily irradiated silicon at low temperatures, looking forward to sensors capable of withstanding fluences up to 10^{16} n/cm^2.

b. Lorentz shift in silicon detectors at low temperatures

Operation of silicon sensors in a magnetic field has to take into account the Lorentz shift due to the presence of a magnetic force acting upon the carriers, proportional to drift velocity, which can result in a displacement and spreading of the charge cloud inside the sensor with the consequence of degrading the spatial resolution of highly segmented devices. This effect is stronger with intense magnetic fields (4 T or more) and has a dramatic increase at low temperatures because of the higher carrier mobilities allowing drift velocities close to saturation values. A good understanding of the Lorentz shift in silicon sensors is therefore

mandatory for operating segmented devices at cryogenic temperatures in strong magnetic fields.

The Lorentz shift has been measured for temperatures down to 80 K using a TCT setup placed inside a superconducting magnet at Forschungzentrum Karlsruhe. Measurements were performed with double-sided HERA-B minisensors with a pitch of 50 μm on the p-side and 80 μm on the n-side; sensors were read out by a 128-channel charge sensitive chip (PREMUX) and a VME-based readout system. A red laser was used to generate charge carriers on both the p- and the n-sides of the sensor, and then the barycentre of the signal distribution on the opposite side was evaluated for different magnetic field intensities up to 8 T, and taken as the central position of the collected carrier charge cloud (see Fig. 5.1 from ref. [2.7]). At 4 T field the results show a Lorentz shift smaller than 200 μm for temperatures above 170 K, easily correctable in a tracking algorithm, but for lower temperatures this shift grows significantly, becoming 850 μm at 80 K. Results with a more penetrating infrared laser, generating carriers throughout the whole sensor thickness, showed that because of the drift of both types of carriers under the magnetic field, the Lorentz shift was about a factor 2 smaller that one only one carrier was injected with the red laser.

In order to model and understand the Lorentz shift from room temperature down to 77 K, the drift mobilities and the saturation velocities of carriers was measured for pad diodes at different bias potentials and temperatures. Also, the Hall factor r_H was calculated giving results in good agreement with the literature, namely $r_H \approx 1.0 \pm 0.1$.

For modeling the temperature dependence of the Lorentz shift, two approaches were followed: a simple model based only the drift mobilities, saturation velocities and Hall factor; and a more sophisticated model considering the microscopic flight and random scattering of carriers, taking into account the anisotropic energy surface of silicon crystals. This second model was successful in describing the data features in the whole temperature range, with the conclusion that random scattering and a finite probability of long free flights are the main effects causing the high Lorentz shift at low temperatures. For details see reference [2.7] and Fig. 5.15)

c. Carrier lifetime measurement using microwave absorption technique

It is essential to understand the carrier lifetimes and parameters of the radiation defects created *in-situ* in cryogenic environment. Issues significant in the development of suitable instrumentation were studied during the last period.

The sensitivity and dynamic range of the microwave absorption by free carriers technique were investigated for applications with heavily irradiated Si detectors. Different experimental geometries were tested in irradiated Si diodes. It has been established that it is possible to detect radiation defects active for recombination at concentrations in the range from $8 \cdot 10^{11}$ to $>10^{16}$ cm^{-3} in silicon with medium and high resistivity.

Excess carrier lifetime τ variations with fluence Φ of different particles of high energy have been investigated to clarify competition between native and radiation-induced defects. Using samples irradiated with particles of different energies, the possibility to monitor depth distribution of radiation-induced defects has been examined. For instance, in γ-ray irradiated samples the native material and sample structure defects govern the recombination characteristics of particle detectors, while in the same diodes irradiated by high energy

protons the carrier effective lifetime is mainly determined by radiation defects (Fig. 2.10). The generalized dose dependence obtained in samples irradiated by different particles is demonstrated in Fig. 2.11. The dominant role of irradiation dose in producing the radiation defects can be deduced. For instance, implantation processes enable to achieve the most significant carrier lifetime variations up to Si material amorphisation, while thin damaged layer resides near the surface. In the relatively narrow dose ranges, the inverse carrier lifetime increases linearly with the irradiation fluence Φ, and allows to estimate the defect introduction rate by using the parameter $\partial\tau^{-1}/\partial\Phi$ as a proper factor. Temperature dependences of carrier lifetime were measured to clarify the dynamic range of lifetime changes probable in cryogenic environment. It has been established that carrier trapping effects can be pronounced in the range of low temperatures.

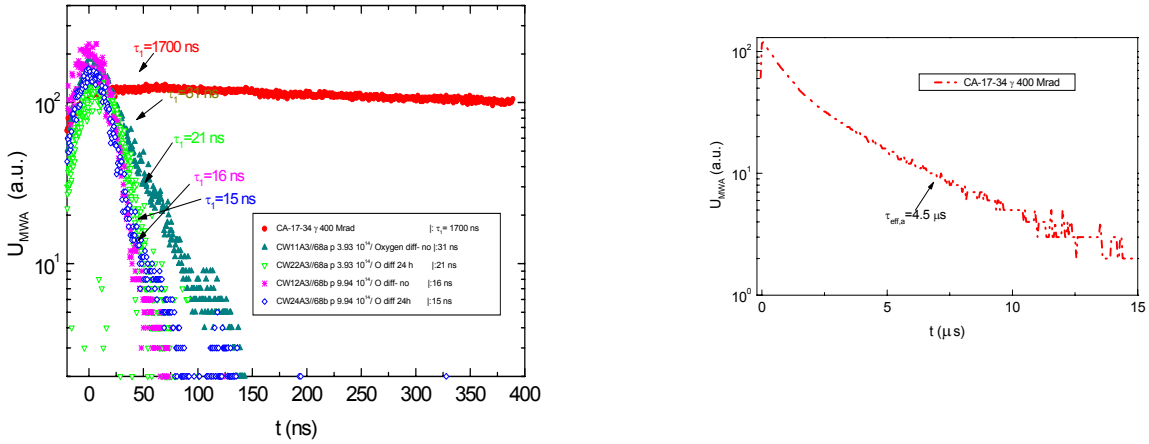

a) b)

Fig. 2.10 Fast and single componential decays have been observed in proton irradiated diodes (a) while in γ irradiated diode components of bulk and surface recombination can be separated, as bulk lifetime is relatively long (b). The decays are measured keeping nearly the same excitation intensity at 1064 nm light wavelength. Absolute values of excess carrier concentrations at the same exxcitation intensity are found in un-annealled (O diff no) diodes to be higher than those of annealed. A lifetime decrease with irradiation dose can be noriced, but for the highest fluences the lifetime values approach to resolution threshold of the MWA instrument.

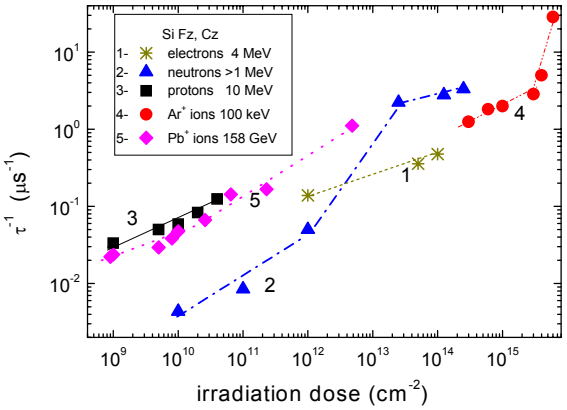

Fig. 2.11. Experimental dependencies of the inverse carrier lifetime on irradiation dose of electrons (1, 4 MeV), neutrons (2, 1 MeV), protons (3, 10 MeV), Ar ions (4, 100 keV), and Pb ions (5, 158 GeV).

It has been clarified from the above mentioned research that the available range of the time span should be widened towards short lifetimes to measure reliably the recombination parameters in the sub-nanosecond scale for heavily irradiated diodes. The necessity of synchronous additional CW bias illumination during carrier lifetime measurements at cryogenic temperatures has been established to separate parameters of excess carrier recombination and of trapping. Therefore, a lot of problems arising in waveguide circuit engineering, in vacuum and cryogenic insulation as well as microwave signal recording, and in optical excitation schemes were examined during these investigations.

d. Space charge evolution during TSC and DLTC measurements

It has been shown recently by our Florence group that during the measurements of radiation induced defects (TSC and DLTS in their case), the space charge density and sign will charge with temperature during the measurements, as shown in Fig. 2.12. Although in TSC and DLTS measurements, where filling of traps via charge/current injection has taken place, the space charge density is not the same as that in thermal equilibrium, this change of space charge with temperature gives independent approve to the fact that the space charge density and sign can be manipulated at various low temperatures, and it points out that one has to take great care of the true space charge density before determining the defect density during the TSC and DLTS measurements. For more details, please see ref. [2.8].

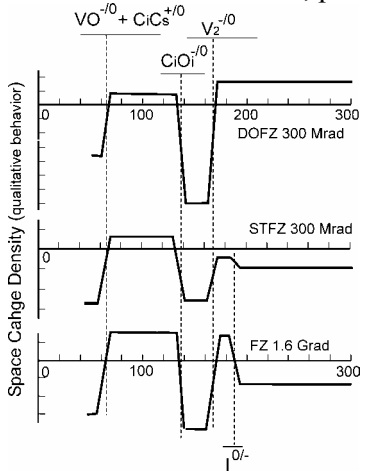

Fig. 2.12 Space charge evolution with temperature during the TSC and DLTS measurements.

e. Spin-dependent recombination electron paramagnetic resonance spectroscopy of radiation induced defects

It has been demonstrated by RD39 that the Spin-dependent recombination (SDR) electron paramagnetic resonance (EPR) spectroscopy is a powerful tool to study radiation-induced defects at low temperatures (T<100 K) [2.9]. At temperatures below 100 K, the SDR-EPR spectra are well observable by measurements of the microwave conductivity or by detecting a DC forward current I_F below a forward-blocking potential. In irradiated FZ Si detectors, the main defects measured by the SDR-EPR have been identified as the complex of two substitutional carbon atoms and one interstitial Si atom (C_s-Si_i-C_s) and the A-center (O-V,

oxygen-vacancy center). At T<100 K, in spite of the low concentration of oxygen in FZ Si, the A-center is found to play an important role in the recombination process in the detector. Details of measurement techniques and defect spectra can be found in ref. [2.9].

REFERENCES OF SECTION 2

[2.1] V. Eremin et al, The charge collection in single side silicon microstrip detectors, Nucl. Instr. & Meth. A 500 (2003) 121-132.

[2.2] V. Eremin et al, The returned charge effect in Si microstrip detectors, accepted by Nucl. Instr. & Meth. A for publication.

[2.3] E. Verbitskaya et al, The effect of charge collection recovery in silicon p-n junction detectors irradiated by different particles, NIM A (in press).

[2.4] B. Dezillie, V. Eremin, Z. Li and E. Verbitskaya, "Polarization of silicon detectors by minimum ionizing particles", Nucl. Instr. Meth. In Phys. Res. A, vol. 452, pp. 440-453, 2000.

[2.5] V. Eremin, E. Verbitskaya, I. Ilyashenko, Z. Li, T. O. Niinikoski and G. Ruggiero, "Temperature dependence of charge collection efficiency in heavily irradiated silicon detectors: the Lazarus effect model", Nucl. Instr. Meth. In Phys. Res. A, in press

[2.6] P. Rato Mendes, M. C. Abreu, V. Eremin, Z. Li, T. O. Niinikoski, S. Rodrigues, P. Sousa, E. Verbitskaya, "A new technique for the investigation of deep levels on irradiated silicon based on the Lazarus effect", oral presentation at the IEEE NSS/MIC 2003, Portland (OR), USA; submitted to IEEE Trans. Nucl. Sci.

[2.7] A. Dierlamm, Ph.D. Thesis, Karlsruhe Univ.-2003, Report # IEKP-KA/03-23

[2.8] D. Menichelli et al, presented at the Florence Conference, August, 2003, Florence, Italy; to be published in Nucl. Instr. & Meth. A.

[2.9] V. Eremin et al, Spin-dependent recombination electron paramagnetic resonance spectroscopy of defects in irradiated silicon detectors, J. Appl. Phys., Vol. 94, No. 1 (2003) 9659.

3 CRYOGENIC MODULES

3.1 High-energy beam test results of edgeless detectors

Measurements in X5 beam

The development of edge cutting and etching techniques for p-i-n silicon detectors were reported in our previous Status Report [3.1], and the positive results of the production of such "edgeless" sensors were already published [3.2]. This work was motivated by the measurement of the very forward elastic scattering at the CERN LHC, needed in the luminosity-independent measurement of the total cross section [3.3,3.4]. This measurement also yields the value for the luminosity itself, enabling the calibration of luminosity monitoring detectors that are simpler, faster and operational at full luminosity.

A pair of edgeless silicon diode pad sensors (Figure 3.1) cut through their p^+ implant at BNL using dicing and chemical treatment techniques as described in [3.2], was exposed to

the X5 high energy pion beam at CERN, in order to determine the edge sensitivity. The signal of the edgeless detector pair triggered a reference telescope made of silicon microstrip detector modules. The setup is shown schematically in Figure 3.2.

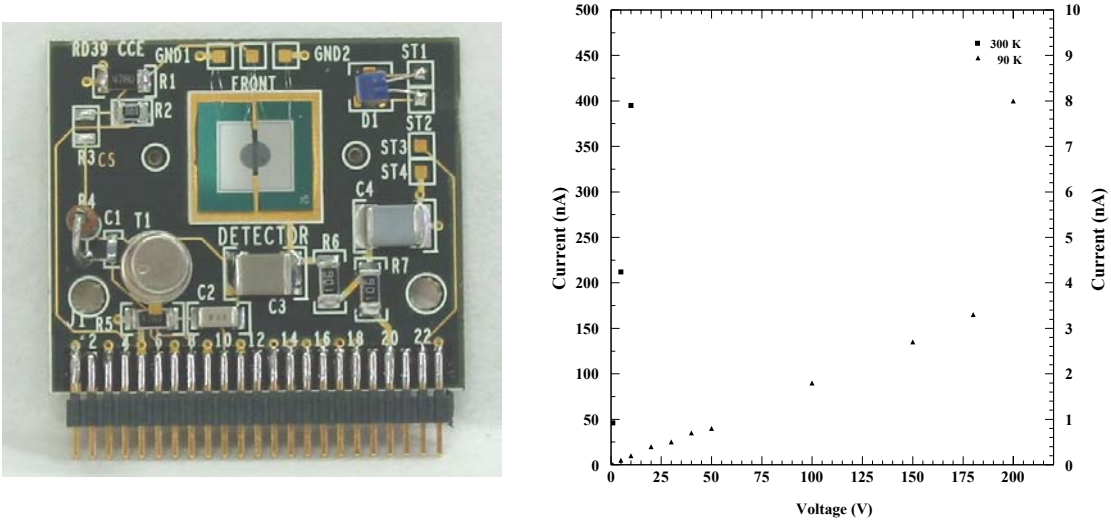

Figure 3.1: Left: Pair of edgeless diodes mounted on a PC, with a gap of about 0.45 mm between treated edges of the devices. Right: The V-I characteristics of the measured edgeless diode at RT (left scale) and at 90 K (right scale), showing that the edge current can be sufficiently reduced at bias potentials well in excess of the full depletion potential of about 40 V.

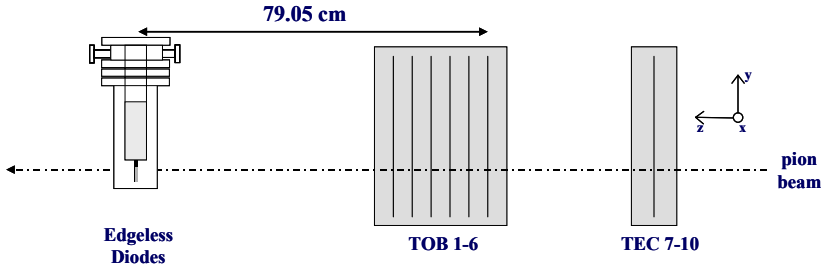

Figure 3.2. Experimental setup

The results of three main runs, where the edgeless diodes were biased to 50 V, 100 V and 150 V, are shown in Table 3.1. The parameters were obtained by fitting a model function to the *x*-distribution of the tracks at the *z*-position of the edgeless trigger diodes. The model function is a convolution of the Gaussian shape of the beam with the gap function, which is a sum of two Heaviside functions convoluted with the effective edge resolution function, assumed also to be Gaussian. The quality of the fit is illustrated by Fig. 3.3, showing the *x*-distribution and the fit of the model function for the data collected at 100 V bias potential.

Parameter	Symbol	Units	U_{bias} = 50 V	U_{bias} = 100 V	U_{bias} = 150 V
Number of tracks			30659	491861	226486
Beam normalization	B		1334±13	23360±63	10284±42
Beam center	μ_B	cm	–3.201±0.013	–3.373±0.001	–3.334±0.001
Beam width	σ_B	cm	0.299±0.086	0.190±0.001	0.190±0.001
Gap width	d_g	μm	435±14	463±3	389±5
Effective edge resolution	σ_g	μm	180±7	180±2	162±3
Gap center	μ_g	cm	–3.335±0.006	–3.325±0.001	–3.316±0.001

Table 3.1: Results of the fits for the three runs at different bias potentials.

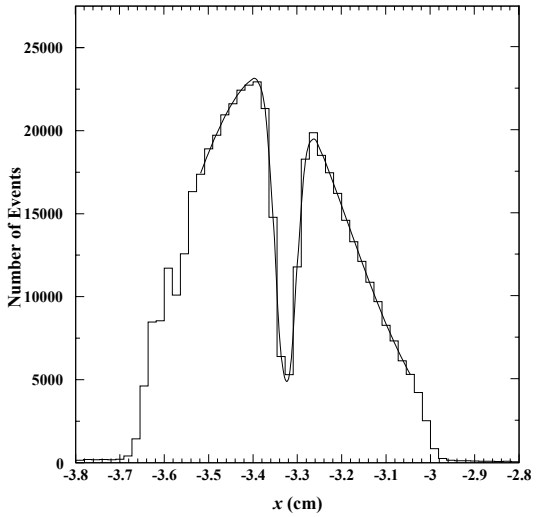

Figure 3.3. The x-distribution of the extrapolated tracks on the plane of the pair of edgeless diodes. The bias potential is 100 V.

The statistical errors in the effective gap width measured by the beam are quite small, as was shown in the Table 3.1, thanks to the relatively good statistics. The main systematic errors are due to approximations in our model function, and to the fact that the bins are quite large compared with the gap, owing to the pitch of the tracker modules. The statistical and systematic sources of error are summarized in Table 3.2.

Error source	**Units**	**Bias potential U_{bias} (V)**		
		50	**100**	**150**
Fit (stat.)	μm	14	3	5
Non-gaussian beam (syst.)	μm	4	4	4
Non-gaussian tracker resolution (syst.)	μm	7	2	3
No convolution of the beam (syst.)	μm	5	5	5
Sum of systematic errors	μm	16	11	12

Table 3.2: Statistical and systematic errors of the effective gap width d_g. The systematic errors are summed in a linear manner.

The gap measurement on the metrology table has a measurement error (±3 μm), and there is also an error due to non-parallelism of the edges. The average width of the gap, weighted by the relative beam intensity is $418 \pm 11_{stat.}$ μm.

This result of the gap measurement on metrology table, together with the above results of the measurement of the effective gap by the beam as a function of the bias potential, are shown in Figure 3.4. There seems to be no systematic variation of the effective gap width as a function of the bias. Although we don't know the exact cause of the deviation of the point at 100 V, which is slightly more than 3 standard deviations above the optically measured gap, we speculate that this could be due to the mechanical instability of the experimental set-up, which shows up more in the long runs with high statistic. This is obvious also in the variation of the absolute position of the gap, and in the variation of the effective edge resolution, as shown by the results of the Table 3.1.

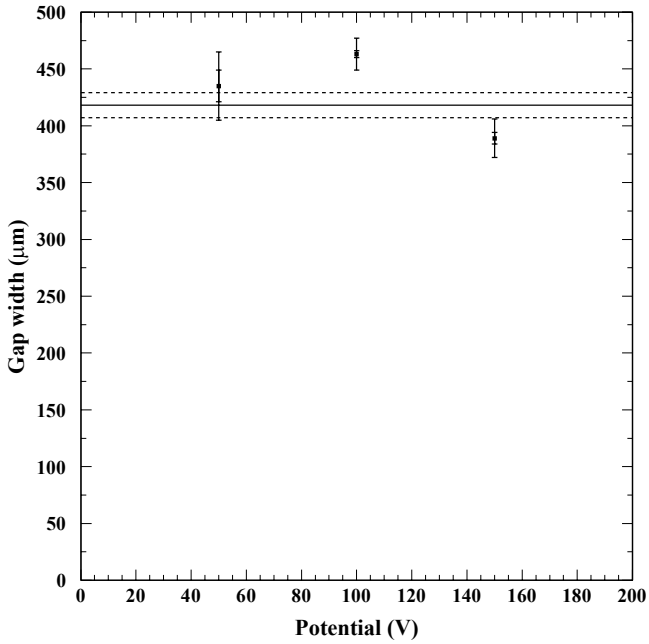

Figure 3.4: Comparison between metrology and beam measurements of the gap width between the pair of edgeless diodes. The horizontal line shows the optically measured average gap width, with its statistical error limits shown by dashed lines. The data points refer to beam measurements at different bias potentials. The smaller bars on data points show their statistical errors, and the larger ones the sum of the statistical and systematic errors.

The effective gap measured by the beam on one hand, and the gap measured on the metrology table on the other, can now be compared, in order to estimate the size of the insensitive layer of silicon at the edges of the devices.

Since there is no evidence of systematic dependence of the gap width with the bias potential, which seems logical since the diode is fully depleted already at 50 V, the effective gap measured with the beam can be calculated as an average weighted with the squared standard deviations of the measured values. This average is $(443 \pm 3_{stat.} \pm 11_{syst.})$ μm. By subtracting from this the value of the gap measured on the metrology table, the sum of the

average thicknesses of the two insensitive layers at the edges of the detectors is ($25 \pm 12_{stat.} \pm 11_{syst.}$) μm.

If the insensitive layers have even and equal thicknesses, the dead layer thickness in this case is ($12.5 \pm 8 \pm 6$) μm. We can therefore conclude that the experimental thickness of the dead layer is compatible with zero within the statistical error of 8 μm and within the systematic accuracy of 6 μm.

A full account of this work is given in our forthcoming paper [3.5].

Measurements in H2 beam

A series of edgeless diode pairs was prepared for tests in the H2 beam, in view of improving the precision for the knowledge of the signals coming from the edge region. The equipment consisted of the pair of edgeless diodes and of the reference tracker of Helsinki Institute of Physics, which has 8 microstrip detector modules with 50 μm pitch. Rather than using the edgeless diodes for triggering the telescope, the diode signals were converted by an ADC and stored together with the tracker event data. The apparatus was triggered by scintillators, which were larger than the edgeless diode pair.

Unfortunately the SPS had very little effective beam time available in August and September of 2003, and our tests could not be carried out reasonable in the parasitic mode of running in the H2 beam.

Edgeless micro-strips detectors

RD39 is also studying the efficiency of the edgeless silicon micro-strips detectors at low-temperature as tracking sensors for several applications, including imaging and particle detection very close to an intense beam. In these conditions, the space surrounding the strips regions that is inefficient for particles detection has to be limited at minimum. For this purpose, single sided micro-strip detectors were chosen. These were fabricated on n-type FZ silicon substrates of 320 μm thickness, using the CMS design. These baby-sensors have 196 strips with 120 μm pitch. The sensor surface covered by the strips is 2.5×2.0 cm^2. They were divided in 3 groups in order to be cut in different geometries at Brookhaven National Laboratory.

- two baby-detectors with the substrate doping concentration around $1.85 \cdot 10^{13}$ cm^{-3}, corresponding to a full depletion bias potential V_{fd} around 124 V, were cut straight, along the border strip, through the p^+ implant;
- two baby detectors with the substrate doping concentration around $1.49 \cdot 10^{13}$ cm^{-3}, corresponding to a V_{fd} around 100 V were cut at an small angle formed by the strips with the cut line, without further etching process;
- one baby detector was cut with a 3 mm hole in the middle of the detector with a silicon etching process afterwards; this baby detector depleted before cut at around 121 V.

We measured the sensors leakage current up to 300V for all detectors at –10°C before and after cut, and also at –50°C after the mechanical cut. We followed this procedure in order to be able to separate the leakage current component that depend by the temperature from the one that is less temperature dependent and comes up from the silicon crystal damage. The detectors are now ready to be mounted on a cryogenic module with CMS readout electronics.

3.2 Assembly and tests of cryogenic microstrip detector modules

An extensive test program was carried out in order to study the cooling and thermo-elastic properties of cryogenic modules assembled according to the principles, which were already discussed in our previous Status Report [3.1]. In this design silicon is used also as a structural material, in order to avoid mismatch between the thermal dilatations between different materials. Another deviation from the classical radiation-hard LHC module designs is the cooling, which uses a micropipe integrated in the module structure between the sensor and the readout hybrid. We shall report here the main conclusions from the above work done during the last 20 months.

Cooling by 2-phase flow in micropipes

Miniaturized fluid circuits with two-phase flow and active circulation of the coolant enable medium-power cryogenic cooling distribution over large distances with low losses, and yield the best performance and the highest degree of integration in a device. A system was designed and constructed for studying the micropipe heat transfer and flow friction, and for developing the engineering rules for upscaling. The system comprises of a room-temperature compressor, built of off-the-shelf industrial components, a Gifford-McMahon cryocooler, and a vacuum chamber housing the devices under test [3.6].

Extensive experimental investigations on heat transfer in microtubes were conducted with argon at about 120 K, using microtubes of 250 μm and 500 μm inner diameter. The results in single-phase heat transfer revealed no fundamental differences between microtubes and macrotubes. The enhancement of single-phase heat transfer, compared with conventional correlations, was attributed to the increased influence of roughness, and was modeled with a newly defined roughness parameter.

In nucleate boiling heat transfer, an extension of the diameter dependence in the VDI Heat Atlas [3.7] correlation for vertical tubes was proposed. Concerning critical boiling conditions, the phenomenon of thermal runaway caused by local dryout was observed and recorded. The stability of evaporative microtube cooling was proved by experiments, and the stability limits were explored.

The results and conclusions of the above work are reported in the Thesis of Steffen Grohmann [3.8]. It was seen that the mass flux and vapour fraction have no significant influence on the nucleate flow boiling heat transfer, which agrees with the VDI Heat Atlas correlations, except for the dependence on pipe diameter. An extension of the diameter function was proposed, based on the Laplace constant. The extended function becomes effective when the tube diameter is in the range of the bubble departure diameter from the wall.

The stability criteria developed in this work suggest that a wide parameter domain exists for stable operation. Operating conditions close to the boiling line should be avoided, however.

The design rules for microchannel heat exchangers are based mainly on the heat flux, which should be high. Short exchangers with large diameter are favourable, and many exchangers in series is better that many exchangers in parallel. Expansion from subcooled fluid to the two-phase regime, right before the series of exchangers, is the best way of stabilizing the flow and the heat transfer. If the main source of heat in the module is the CMS

hybrid, and a cooling pipe of 500 μm diameter is chosen, about 15 modules can be cooled in series if the available pressure head is 2 bar to 3 bar, and operating temperature around 130 K.

Thermal and thermo-elastic module design studies

Several models describing epoxy matrix composite properties predict a lower thermal dilatation coefficient and higher Young modulus for epoxies that are charged with low thermal dilatation particles. Measurements of the thermo-elastic properties of several filled radiation-hard epoxy resins were therefore compared with these theoretical models [3.9].

The integral thermal dilatation of pure Araldite 2011, Stycast 1266 and R&G Type L epoxies was been determined as a function of temperature. Filling of these epoxies with fused quartz powder dramatically reduces their thermal dilatation, nearly matching that of metals. At equal filling factors, R&G Type L shows a larger reduction of the thermal expansion than the other epoxies.

The Kerner model [3.10] seems the best for predicting the dependence of the Young Modulus of the composite with the filling factor. The tensile tests confirm that pure epoxies become brittle at low temperatures, where their Young Modulus increases and the elongation at break is reduced. Similar effects are found when filling the epoxy. The ratio of the coefficient of thermal dilatation of the filled and unfilled epoxies does not seem to follow any of the theoretical models.

It turns out, however, that the smaller mismatch between the epoxy and silicon is overcompensated by the large increase in the low-temperature Young modulus in the filled epoxies. ANSYS simulations show that thin unfilled epoxy layers would induce smaller stresses in the silicon, compared with filled epoxies. The best glue turned out to be pure Araldite 2011, which was used in the construction of modules for thermal and electrical tests.

A series of test joints comprising of two 400 μm thick silicon wafers glued together with pure Araldite 2011 was fabricated, with different thickness of epoxy. The samples were thermally cycled 10 times down to 80 K. It was found that a critical thickness of about 400 μm causes the silicon to break in the first cooldown.

Construction and tests of cryogenic modules with large sensors

A series of small dummy modules was assembled for thermal tests. The results show that the ANSYS simulations, reported in [3.1], correctly described the thermal map of the module. Two-phase argon at 120 K was used as a coolant in these tests.

Tooling was also designed and fabricated for modules comprising of a 5 cm x 6 cm single-sided sensor, a ceramic CMS hybrid, and microtube cooling pipe integrated between the base plate and the fan-in. One module was successfully assembled and wire bonded, using real components which were electrically non-functional, but mechanically and electrically qualified for mechanical and thermal tests. The module is shown in Figure 3.5.

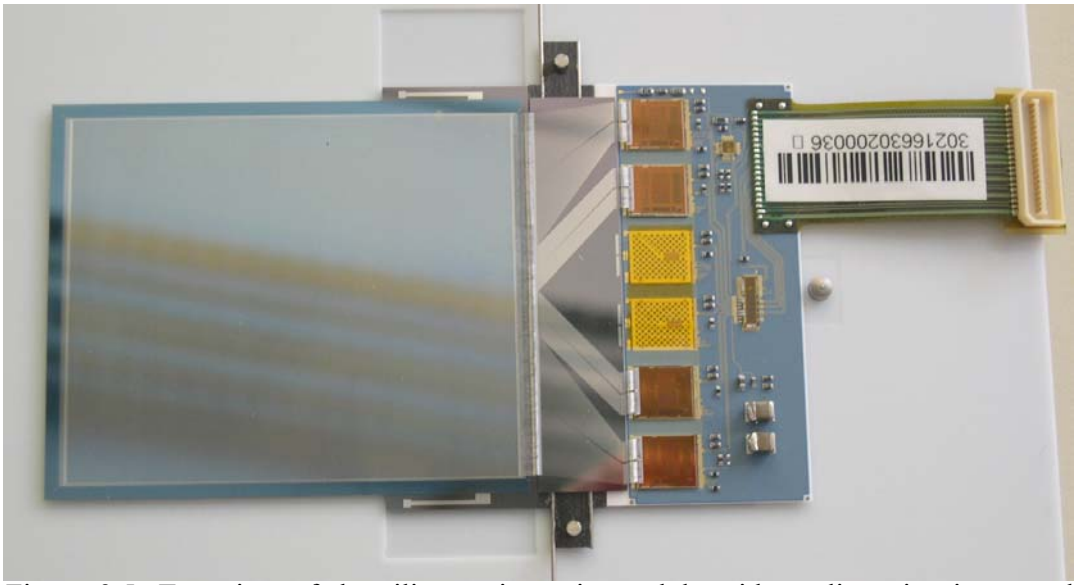

Figure 3.5: Top view of the silicon microstrip module with cooling pipe integrated between the fan-in and the base plate. The size of the sensor is about 5 cm x 6 cm.

The CMS hybrid features a narrow frequency range for the VCO of the PLL chip. Because of acceleration of the DSM circuits at low temperatures, the center frequency of the VCO shifts higher at lowered temperatures, so that the PLL loses its ability to lock to the standard 40 MHz clock frequency of the CMS tracker at about –40 °C temperature. It was therefore decided to fabricate a simple LN2-cooled test chuck for characterizing the hybrids at low temperatures prior to mounting them on the electrical modules. The apparatus is now ready, together with interface boards and CMS test software, and the tests are starting at the time of writing this report.

REFERENCES OF SECTION 3

[3.1] K. Borer et al., RD39 Status Report, CERN CERN/LHCC 2002-004 (2002).

[3.2] Zheng Li et al., IEEE Transactions on Nuclear Science **49** (2002) 1040 .

[3.3] U. Amaldi *et al*., Precision measurement of proton-proton total cross-section at the CERN Intersecting Storage Rings, Nucl. Phys., B145, 367-401 (1978)

[3.4] W. Kienzle *et al*., TOTEM Technical Proposal, CERN/LHCC 99-7 (1999)

[3.5] B. Perea Solano, *Edge sensitivity of "edgeless" silicon pad detectors measured in high energy beam,* to be submitted to Nucl. Instr. & Meth. A.

[3.6] S. Grohmann et al., *in* Proc. ICEC 19, Ed. G. Baguer and P. Seyfert, (Narosa Publishing House, New Delhi 2003) p. 411.

[3.7] S. Grohmann, *Distributed cooling in cryogenics with miniaturized fluid circuits*, Thesis for the degree of Dr.-Ing. (Technical University of Dresden, 2003).

[3.8] *VDI Wärmeatlas* (VDI Verlag, 1991).

[3.9] B. Perea Solano, T. Niinikoski, S. Grohmann and G. Vandoni, *in* Proc. ICEC 19, Ed. G. Baguer and P. Seyfert, (Narosa Publishing House, New Delhi, 2003) p. 705.

[3.10] E.H. Kerner, Proc. Phys. Soc. **69 B**, 808-813 (1956)

4 RD39/COMPASS

In the framework of RD39, the work of COMPASS is related to the implementation in the experiment of silicon detectors, operated at cryogenic temperatures.

Shown in Fig. 4.1 is the cold detector setup in the M2 beam of COMPASS. The detector used is a double-sided 280μm thick detector, developed for HERA-B experiment, $7\times5cm^2$ active area. The detector is glued between two L-shaped PCB boards, each of them hosts the readout for one side of the detector. The readout chip used is the APV25-S1, designed for CMS. The cooling is performed via liquid nitrogen, fluxing in capillaries soldered to the boards. Further information about the detector, the electronic and its usage in COMPASS can be found in [4.1].

This year, our main task was to install in the experiment one cryogenic station, which is two detectors operated at 130K. The goal was achieved at the end of July, when the station took data for several days. Unfortunately, due to the presence of frozen water in the nitrogen supply it was not possible to operate the station for longer time, proving the feasibility of the project. We also faced several other problems, the solution of which will be a challenging task for the preparation of the 2004 run.

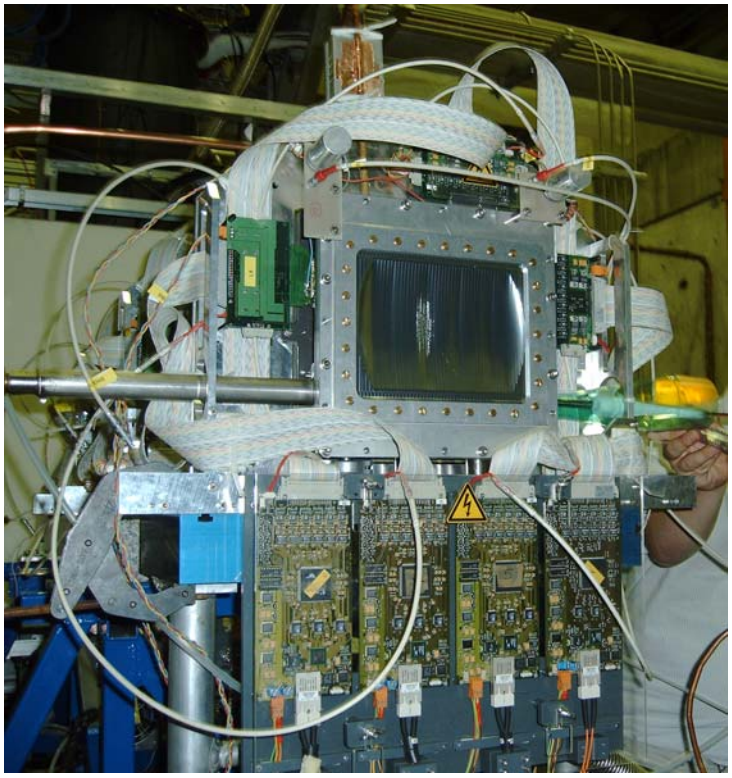

Figure 4.1 Cryogenic detector setup in the SPS M2 beam of COMPASS

REFERENCE OF SECTION 4

[4.1] H. Angerer et al., “Present status of silicon detectors in COMPASS”, Nucl. Instr. And Meth. In Phys. Res. **A 512**, 229 (2003)

5 FUTURE PLANS FOR RD39

5.1 Device Physics and Basic Research

These continue to be coordinated by Vladimir Eremin (Device Physics) and Pedro Rato Mendez (Basic Research).

Many advantages arise from the cryogenic operation of the Si detectors in heavy radiation environment such as LHC and upgrade:

- No leakage current (low electrical power from HV supply)
- Low depletion voltage (original Lazarus effect)
- Fast charge transit (higher carrier drift mobility)
- CCE increase without reduction of detector thickness (increase of charge collection depth) due to the freeze-out of trapping as will stated below
- Readout electronics becomes faster and has lower noise
- Thermal stability of sensors is improved (higher thermal conductivity of Si, no leakage current)

For LHC upgrade, with an increase in luminosity by one order of magnitude, the maximum fluence for detectors close to the interaction point can be as high as 10^{16} n_{eq}/cm^2 (n_{eq}: 1 MeV neutron equivalent) over 10 years. With such extremely high radiation level, the CCE of Si detectors is limited not only by the electric field distribution in the detector ($N_{eff}(x)$), but also by the trapping of free carriers by shallow trap centers. The detector CCE is: $CCE = CCE_{GF} * CCE_t$, where CCE_{GF} is the geometry factor that is affected by detector full deletion voltage V_{fd} and the second term CCE_t is the trapping factor that is related to the trapping of carriers by trap centers. As demonstrated by the previous RD39 results [3.1], the CCE_{GF} can be increased close to 1 by manipulating the electric field in the detector via current and/or charge injection at temperatures from 130 K to 150 K. Since for fluence less than10^{15} n_{eq}/cm^2, the trapping effect on the term CCE_t is insignificant, CCE can be significantly improved by improving only the CCE_{GF} at temperatures from 130 K to 150 K. This is in fact the original "Lazarus" effect. However, for extremely high fluence (10^{16} n_{eq}/cm^2) in LHC upgrade environment, the trapping term can also be significantly degraded by the trapping effect thus affecting the CCE greatly.

For LHC upgrade fluence 10^{16} n_{eq}/cm^2, the trapping time constant in Si is about 0.2 ns. So even for detectors operated at the highest bias voltage for which the carrier saturation velocity of 10^7 cm/s is reached, the mean free path of a carrier generated by MIP before it is trapped a trap level is about 20 μm. In other words, electron-hole pairs can only be separated by 20 μm before they are trapped. Therefore, even if a detector with d = 300 μm is fully depleted, the effective charge collection distance is only 20 μm, which gives a CCE_t = 20/300 = 0.07 or 7% at 10^{16} n_{eq}/cm^2. This implies that the charge collected by a detector with 20 μm thickness would be the same as that collected by a detector with thickness >20 μm even if they are all fully depleted. This is the reason to use thinner detectors for extremely high radiation fluence. For example, at 10^{16} n/cm^2, for a detector with a thickness of 40 μm, the CCE_t = 20/40 = 50%. However, the signals obtained from thinner detectors are greatly reduced, leading to much lower S/N ratio.

The detrapping of trapped carriers depends very strongly on the temperature. This dependence makes it possible to freeze-out trapping centers at low temperatures. If a trap level is filled (say, by current or charge injection) and then frozen (very long detrapping time) at cryogenic temperatures, this trap level will no longer be able to trap free carriers again. The trap in fact becomes electrically inactive while it is occupied. In this case, the CCE_t can be improved as well to a value close to 1, and therefore significantly improve the CCE. Since trap levels are normally shallow, one has to go to cryogenic temperatures to freeze them out. The most dominant, radiation-induced trapping center in Si, for example, is the A-center (O-V) at E_c–0.18 eV with capture cross section of 10^{-15} cm^2. For the A-center, the detrapping time constants at various temperatures are listed in Table 5.1.

T(K)	300	150	100	77	60	55	50	45	40
τ_d(s)	$1.0x10^{-11}$	$1.1x10^{-8}$	$1.10x10^{-5}$	$5.8x10^{-3}$	12.3	291	$1.3x10^4$	$1.3x10^6$ (15 days)	$4.3x10^8$ (13 years)

Table 5.1 Detrapping time constant for the A-center at various temperatures

It is clear that already the A-center is freeze-out for 10's of seconds at T=60 K. At T=45 K, the A-center will be frozen for 15 days after filling, and for 13 years at T=40 K. So if one fills the A-center at T=40 K, it will not be active as a trapping center for the next 13 years! Even at higher temperatures, sat at T=45 K, one may need to fill the A-center every 15 days, which can be easily done.

As one of the main task for RD39 for the next few years, we will work on the heavily irradiated Si detectors at various cryogenic temperatures below LN_2 temperature (77 K). We will systematically measure detector CCE at these temperatures with MIP (β source) and TCT technique (ps laser) to identify the characteristic temperature(s) at which all trapping centers will be frozen out. We expect that by operating Si detectors at such characteristic temperatures, the detector CCE can be greatly improved without reducing the detector thickness.

RD39 has now some set of pad samples either already been irradiated or being irradiated by high energy and low energy protons up to fluence of $1x10^{16}$ n_{eq}/cm^2, as listed in Table 5.2. Segmented detectors (microstrip and pixel detectors) will be irradiated in a few months also up to $1x10^{16}$ n_{eq}/cm^2.

In the short to medium term program, pad detectors will be studied by TCT and CCE techniques to temperatures lower than 80 K to identify the specific temperature at which the trapping can be freeze-out. We will build new setups (see 5.4 below), including TCT, CCE, and in situ lifetime measurement, with cryostat capable to cool samples down to LHe temperature. With these new setups, we can for the first time test and study Si detectors down to temperatures lower than LN_2 temperature.

Material	Source	Fluence	Structure	Responsible Institute
FZ, n and p	24 GeV p	Up to 10^{16}p/cm^2	p/n/n p/n/p n/p/p	PTI
MCZ CF FZ Oxy. FZ	10-50 MeV p	Up to 10^{15} n_{eq}/cm^2	p/n/n	HIP
MCZ	27 MeV p (Karlsruhe)	Up to 2x$10^{16}$$n_{eq}$/cm^2	p/n/n	BNL
FZ	27 MeV p (Karlsruhe)	Up to 1x$10^{16}$$n_{eq}$/cm^2	p/n/n	BNL

Table 5.2RD39 samples irradiated to very high fluences for future studies for SLHC

The following tasks will be carried out in the next year:

- Test on the pad detectors using the current injection diode (CID) technique for RT radiation up to 10^{16} n_{eq}/cm^2 (using Karlsruhe low energy protons). Check the electrical field profile with TCT and CCE with TCT and electron source.
- Using pad detectors to study the carrier trapping effect at cryogenic temperatures for detectors irradiated at RT to 10^{16} n_{eq}/cm^2. A possible lower temperature than 80 K may be needed to freeze the trapping centers.
- Using pad detectors to study the carrier trapping effect at cryogenic temperatures for detectors irradiated at cryogenic temperatures (in-situ radiation) to 10^{16} n_{eq}/cm^2. This may allow us study the defect formation and evolution with time at cryogenic temperatures.
- Verification of possible new improvement in CCE at cryogenic temperatures (due to the freezing out of trapping centers, in additional to the modification of electric field, or depletion depth) lower than 80 K on segmented detectors (e.g. micro strip detectors).
- Development and setting-up of a cryostat for studies of detector devices *in-situ* during irradiation in the PS facility. These may include studies of charge carrier relaxation and recombination, and TCT studies.
- Avalanche photodiode studies
- Fast TCT measurements on thin detectors at cryogenic temperatures up to 10^{16} n_{eq}/cm^2. Measurement of electrical field profiles in forward biased and current injected pad diodes and segmented detectors.

5.2 Cryogenic modules

We will characterize the CMS hybrids at low temperatures down to 80 K using our newly fabricated low temperature chuck. The same apparatus will be used for the electrical tests of modules at low temperatures (see 3.2). The modules will then be irradiated by proton beams (PS beam). Source and beam tests of irradiated modules will be characterized and electrically tested again at low temperatures.

5.3 RD39/COMPASS

The main task for the year 2004 is the installation and operation of three cryogenic stations. In order to achieve this goal the following steps are needed:

- Installation of a distribution box for nitrogen, which can serve up to five stations in parallel. Each station can be operated independently from the others. The construction of such box is ongoing.
- Development of an automatic system (slow control) for the regulation of the temperature and of other parameters related to the stations (vacuum, flow rates, etc.).
- Improvement of the mechanical construction, in order to reduce the thermal conductivity.
- Installation of a filter in the liquid nitrogen line.

5.4 Plan for new equipment

In order to study and test Si detectors down to temperatures lower than 80K, new LHe cryostat will be needed for TCT and CCE setups. RD39 plans to request help from CERN, with contributions also from member institutes, to build the following three new equipments in CERN for use the development of ultra radiation-hard Si detectors for applications in LHC and upgrade:

- A Fast TCT setup with fast laser (ps) and fast amplifier, LHe cryostat. The ACAD design will be about 1 month after approval by CERN and construction should immediately follow, and completed in 3 months. Setting, calibration, and testing will be done in one month thereafter
- A CCE setup with a β source and LHe cryostat. Upon approval, the design can be completed in two months, construction completed in five months thereafter, and addition one month for setting, calibration, and testing.
- An *in-situ* Microwave Lifetime Measurement setup with LHe cryostat in the PS. The design will take up to three months upon approval, with additional three months for construction, and one month for setting, calibration, and testing.

5.5 Manpower and financial plan

The resources planned by the Institutes of RD39 for work in the projects of RD39 are summarized in Table 1. These resources for the projects in common with the COMPASS include those spent on the prototyping work, but do not include those for the construction of the final detectors or other components for the experiment.

The Table 1 shows, institute by institute, the number of authors, involvement in the 4 projects, annual funds for RD39 and manpower for RD39. The budgets comprises of capital and operating expenses. The capital costs include equipment purchased in the institutes for their research in the framework of RD39. The operating costs include consumables, travel to collaboration meetings, travel for experimental runs and test runs, travel to related conferences, the annual collaboration fee, overheads, and other possible non-capital expenses such as paid services and consumables. The manpower includes not only the signing authors, but also technical support and administrative persons in the institutes who are not visible in

the operating cost. The manpower numbers are expressed in average Full Time Equivalent (FTE) units during the years 2003 and 2004.

Institute	Authors	Device Physics	Basic Research	Cryogenic Modules	RD39/ COMPASS	RD39 Budget (CHF/year)	FTE In RD39
U. Bern	3		x			2000	0.2
U. Northeastern	5	x	x			5000	1.00
BNL	2	x	x			10000	1.00
U. Brunel	1	x	x			4000	0.20
CERN	5	x	x	x	x	6000	2.00
ILK Dresden	3			x	x	5000	1.00
U. Florence	4	x	x			4000	1.00
U. Geneva	1	x		x		1000	0.15
U. Glasgow	2	x	x			2000	0.50
HIP Helsinki	4	x	x			20000	1.00
U. Karlsruhe	7	x	x			5000	2.00
LIP Lisbon	4	x	x	x		3000	0.75
U. Louvain	3	x		x		20000	1.00
JSI Ljubljana	4	x	x			2000	0.50
TU Munich	2			x	x		
U. Naples	3			x	x	2000	0.50
Ioffe PTI	3	x	x	x		10000	1.50
U. Turku	3	x	x			5000	0.60
U. Vilnius	7	x	x			10000	2.0
Total	66	14	11	7	3	116000	16.90

Table 5.3: Resources of the 19 institutes in RD39, planned for the projects of RD39. For institutes involved also directly in the experiments, the resources for the construction of the final detectors are not included in the figures given for the budget and for the FTE manpower.

5.6 Schedule

The planed schedules for RD39 for the next two years with milestones for the various projects are listed in Table 5.4.

Task name	2004				2005			
	Qtr 1	Qtr 2	Qtr 3	Qtr 4	Qtr 1	Qtr 2	Qtr 3	Qtr 4
Device Physics								
Radiation of pad Si detectors	XXXX							
Radiation of segmented Si detectors		XXXX						
Design for Fast TCT with LHe cryostat (FTCT-LHe)	XX							
Construction for FTCT-LHe		XXXX						
Setting of FTCT-LHe			XX					
Measurements of pad Si detectors using FTCT-LHe			XXXXXXXXX					
Measurements of segmented Si detectors using FTCT-LHe					XXXXXXXXXXXXXXXX			
Modeling of E-field and trapping at low temperatures				XXXXX	XXXXXXXXXXXXXXXX			
CID operation at T<80 K				XX	XXXXXXXXXXXXXXXX			
Basic Research								
Design of CCE setup with LHe cryostat (CCE-LHe)	XXX							
Construction of CCE-LHe		XXXXX						
Setting of CCE-LHe			XX					
Measurements of Si pad detectors with CCE-LHe				XXXXX	XXXXXXX			
Measurements of Si segmented detectors with CCE-LHe						XXXXXXXXXXX		
Design of *in-situ* lifetime setup (ML-LHe)	XXXX							
Construction of ML-LHe		XXXXXX						
Setting of ML-LHe			XXX					
Measurements of Si pad detectors with ML-LHe				XXX	XXXXXXXXXXXXXXXX			
Cryogenic Modules								
Characterizations of CMS hybrids at low temperatures	XXXXXXXX							
Assembly of modules		XXXXXXX						
Electrical tests of modules at low temperatures			XXXXXXX					
Irradiation of modules				XXXXX				
Source and beam tests of irradiated modules				XXXXXXX	XXXXXXXXXXXXXXXX			

Table 5.4: Schedule for the projects of RD39 in 2004 and 2005.